Journal of Materials Chemistry A

ROYAL SOCIETY OF CHEMISTRY

PAPER

View Article Online
View Journal | View Issue

Cite this: J. Mater. Chem. A, 2026, 14, 1770

Crystal structure of $Cu_2Zn(Ge_xSi_{1-x})Se_4$ solid solution: the kesterite to wurtz–kesterite structural phase transition

G. Gurieva, *[a] D. M. Többens, [a] A. Manjon Sanz, [b] V. Rotaru, [cd] C. Hennig, [ef] M. Kirkham, [b] M. Guc [c] and S. Schorr [ag]

Developing low-cost, sustainable, and environmentally friendly top absorber layers for tandem solar cells is essential to advancing photovoltaic technologies and accelerating the transition to renewable energy. In this work, we explore the potential of tetravalent ($Cu_2Zn(Ge_xSi_{1-x})Se_4$) cation mutations in chalcogenide compound semiconductors with the aim of finding a material with increased band gap and reduced structural disorder. A combination of high-resolution synchrotron powder diffraction and neutron powder diffraction was used to determine the atomic positions and monoclinic angles in monoclinic wurtz–kesterite type $Cu_2Zn(Ge_xSi_{1-x})Se_4$ mixed crystals as well as to determine the cation distribution in the crystal structure of Ge-rich kesterite-type and Si-rich wurtz–kesterite type mixed crystals. These investigations enabled us to deduce the structural transition scenario within the $Cu_2Zn(Ge_xSi_{1-x})Se_4$ series. The transition occurs *via* a region where two phases with different crystal structures, tetragonal and monoclinic and thus a different distortion of the coordination tetrahedra, but the same cation distribution within the element specific cation sites co-exist. Thus, the structural transition between the kesterite and the wurtz–kesterite structure within the $Cu_2Zn(Ge_xSi_{1-x})Se_4$ series is a distortion driven transition. The study identifies cation mutation in quaternary chalcogenides as a promising strategy beyond chalcopyrites and kesterites for low cost and environmentally friendly top absorbers in tandem solar cells.

Received 30th July 2025
Accepted 9th November 2025

DOI: 10.1039/d5ta06163f

rsc.li/materials-a

1. Introduction

The pursuit for sustainable, efficient, and affordable photovoltaic materials remains a key challenge in the field of solar energy production. A critical aspect of this effort is the development of low-cost and environmentally friendly top absorber layers for tandem solar cells, playing a vital role in the shift away from fossil fuels and towards a more sustainable energy future. The emergence of compound semiconductors has provided an opening into low-cost fabrication of thin-film solar cells, made possible by these materials' higher absorption coefficients which allow for a reduction in absorber layer thickness, and therefore lead to a decrease in production costs. Earth-abundant and mostly non-toxic elements forming indium free Cu-based multinary chalcogenides make these compounds stand out as more environmentally friendly and economic alternatives, creating a new market of solar energy conversion technology.[1]

Due to its non-toxicity and abundance of the constituent elements, $Cu_2ZnSn(S,Se)_4$ (CZTSSe) is a promising low-cost alternative as absorber layer in critical-raw material free thin film solar cells. A number of new world records were announced recently, the highest being 15.1% PCE (power-conversion-efficiency) in 2024.[2,3] But the low open circuit voltage with respect to the band gap phenomenon continues to be a critical issue. The absorber band tailing caused by the exceptionally high density of Cu_{Zn} and Zn_{Cu} anti-sites causing Cu/Zn disorder[4] is believed to be one of the reasons for the limited open-circuit voltage in CZTSSe-based devices.[5]

One of the ways previously shown to completely block structural disorder, especially the Cu/Zn disorder,[4] is a change of the atomic crystal structure, *e.g.* see ref. 6. In doing so, the stacking sequence of lattice planes perpendicular to the crystallographic *c*-axis has to change, but keeping the structural building block, the $Cu_2ZnC^{IV}X$ tetrahedron (see Fig. 1a). Different cation and anion mutation series were studied for this purpose.[7] One example could be substituting Zn^{2+} by Mn^{2+} in

[a]Helmholtz-Zentrum Berlin für Materialien und Energie (HZB), 14109 Berlin, Germany. E-mail: galina.gurieva@helmholtz-berlin.de
[b]Neutron Scattering Division, Oak Ridge National Laboratory, Oak Ridge, TN 37831, USA
[c]Catalonia Institute for Energy Research (IREC), 08930 Barcelona, Spain
[d]Facultat de Fisica, Universitat de Barcelona (UB), 08028 Barcelona, Spain
[e]Helmholtz-Zentrum Dresden-Rossendorf (HZDR), Institute of Resource Ecology, Dresden, Germany
[f]Rossendorf Beamline (BM20), European Synchrotron Radiation Facility, Grenoble, France
[g]Freie Universität Berlin, Institute of Geological Sciences, 12249 Berlin, Germany

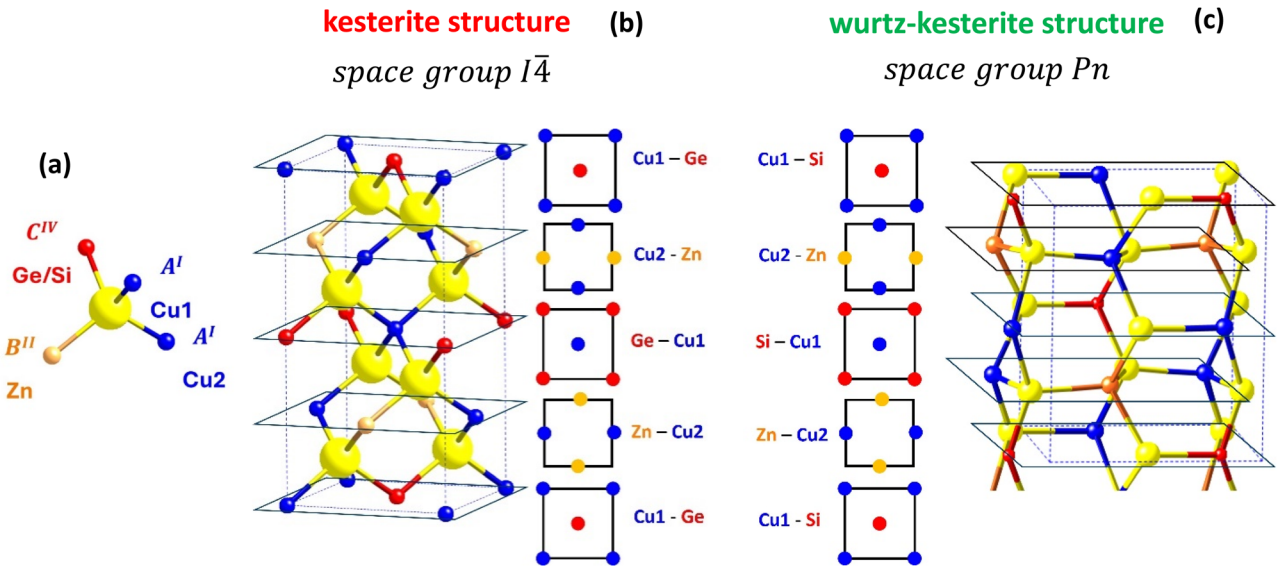

Fig. 1 (a) The anion tetrahedrally coordinated by the cations – the building block of both structures; (b) $Cu_2ZnGeSe_4$ in the kesterite structure with Cu1 on 2*a*, Cu2 on 2*c*, Zn on 2*d* and Ge on 2*b* sites; (c) $Cu_2ZnSiSe_4$ in the wurtz–kesterite structure with Cu1 on $2a_1$, Cu2 on $2a_2$, Zn on $2a_3$ and Si on $2a_4$ sites.

$Cu_2ZnSnSe_4$.[8] In the resulting series, $Cu_2(Zn_{1-x}Mn_x)SnSe_4$, both end members adopt different crystal structures: $Cu_2ZnSnSe_4$ crystallizes in the kesterite-type structure whereas $Cu_2MnSnSe_4$ adopts the stannite-type crystal structure, and both are tetragonal.

Another strategy would be to substitute the tetravalent cation in the $Cu_2Zn(Ge_xSi_{1-x})Se_4$ semiconductor solid solution; in this case, the structural change is even more drastic from a tetragonal structure in $Cu_2ZnGeSe_4$,[9] which was shown to crystallize in a kesterite type structure (space group $I\bar{4}$) (Fig. 1b), to a monoclinic structure in $Cu_2ZnSiSe_4$ (space group *Pn*),[10] which was recently shown by multiple energy anomalous diffraction (MEAD) to be wurtz–kesterite (Fig. 1c). A comprehensive comparison of these two structures can be found in ref. 11, highlighting the changes happening to the $Cu_2ZnC^{IV}X$ anion tetrahedron which is the building block for both structures.

In one of our previous studies,[12] we have shown the crystal structure of $Cu_2ZnGe_xSi_{1-x}Se_4$ mixed crystals in the regions $0 \leq x \leq 0.4$ and $0.6 \leq x < 1$, while the region in the middle of the series ($0.4 < x < 0.6$) was still an open question. Here, we studied the crystal structure, cation distribution and intrinsic point defect scenario through the whole $Cu_2Zn(Ge_xSi_{1-x})Se_4$ series of powder samples by synchrotron X-ray and neutron diffraction at large scale facilities. Applying neutron diffraction enables us to differentiate the isoelectronic cations Cu^+, Zn^{2+} and Ge^{4+} in the crystal structure analysis, which is essential for obtaining insights into the structural phase transition mechanism as well as being able to detect and even more quantify the Cu/Zn disorder. The detailed analysis of the Raman spectra allowed to define the evolution of the main vibrational modes in the solid solutions and to confirm the phase content of the powders. The band gap energy of the studied mixed crystals was deduced from diffuse reflectance measurements.

A proper understanding of the mechanism for the structural phase transition in this solid solution is of uttermost importance for the potential engineering of devices based on these materials. Several questions should be answered in order to achieve such an understanding. These include the details of the transition mechanism from kesterite to wurtz–kesterite structure, the possibility of the existence of Cu/Zn disorder in the wurtz–kesterite structure, and the potential influence over the changes in the band gap.

2. Methodology

2.1 Synthesis, chemical composition and X-ray diffraction

The details of the synthesis, chemical composition determination and the X-ray diffraction analysis of a number of samples (10 powders) from the $Cu_2Zn(Ge_xSi_{1-x})Se_4$ mixed crystal series presented here were published earlier.[12] But the details of crystal structure and the structural transition within the compositional region $0.45 \leq Ge/(Ge + Si) \leq 0.55$ remained an open question. In order to answer this question and close the gap, 6 more powder samples (with $Ge/(Ge + Si) = 0.45$, 0.50 and 0.55) were synthesized additionally. The same synthesis route, the conventional solid-state reaction, was used, but for each group of 3 compositions covering the gap different maximum temperatures were used, 840 °C and 900 °C, respectively. The information on the maximum temperature was included in the sample names and the details of synthesis procedure can be retrieved from SI. The chemical analysis by wavelength dispersive X-ray spectroscopy (WDX) of these 6 new samples was performed in the same way as described in ref. 12.

2.2 Raman spectroscopy

The Raman spectra of a series of $Cu_2Zn(Ge_xSi_{1-x})Se_4$ powders have been measured using a Horiba Jobin Yvon FHR640

monochromator coupled with a CCD detector in a backscattering configuration thorough a probe designed in IREC. The study was performed using the 442, 532 and 785 nm lasers as excitation sources with a power of ≈2 mW, concentrated through an Olympus ×20 objective on a macro-spot with a diameter of about 70 μm, which allowed collecting Raman spectra from several grains. This and the use of an un-polarized light beam allowed minimizing the influence of the crystalline orientation of the grains on the resulting Raman spectra. In addition, the spectra of 9 points for each sample were measured allowing us to obtain an average representative spectrum for each studied sample. The spectra were normalized on the position of the main peak of monocrystalline Si which was imposed to 520 cm^{-1}.

2.3 Synchrotron X-ray diffraction

X-ray synchrotron data for Rietveld refinement were collected under ambient conditions at the Rossendorf Beamline (BM20 – ROBL) at European Synchrotron Radiation Facility (ESRF) using the XRD-1 high-resolution powder diffractometer setup.[13] A radiation energy of 17 038 eV was used; the wavelength was refined to 0.72769(1) Å using LaB_6 NIST 660c as a calibration standard. The samples were mounted in glass capillaries of 0.3 mm diameter; in order to reduce X-ray absorption, they were mixed with ≈70% ground glass. Data were collected in the 2θ range 3–65°, at 3 different positions along the length of each capillary to further improve particle statistics.

2.4 Neutron diffraction

Neutron powder diffraction experiments were performed at the Spallation Neutron Source (SNS, Oak Ridge National Laboratory) using the POWGEN BL-11A powder diffractometer,[14] IPTS 29192. Approximately 3–4 grams of powder samples were loaded in 6 mm diameter vanadium cans and loaded in the POWGEN automatic sample changer. Time of flight (T.O.F) data were collected at room temperature for 3–4 hours. A center wavelength of 1.5 Å was used, covering a *d*-spacing range of 0.485–13 Å.

2.5 Band gap

Diffuse Reflectance Spectroscopy (DRS) measurements were carried out in air under ambient conditions on a spectrophotometer equipped with an integrating sphere – PerkinElmer UV/Vis-spectrometer Lambda 750S. The measurement range was adjusted for this set of samples to 500–1400 nm, with a step size of 1 nm and the counting time of 1 s per step.

3. Results and discussion

The chemical and phase composition of the $Cu_2Zn(Ge_xSi_{1-x})Se_4$ powder samples were measured using the WDX technique and making a statistically relevant analysis by measuring at least 40 points per sample.[12] In all powder samples, the main phase was a homogeneous quaternary $Cu_2ZnGe_xSi_{1-x}Se_4$ (CZGSiSe) mixed crystal with an off-stoichiometric composition, Cu-poor and Zn-poor for $0 \leq Ge/(Ge + Si) < 0.4$ as well as Cu-rich and Zn-rich for $0.4 \leq Ge/(Ge + Si) < 1$, which is consistent with the previous findings about the volatility of Ge during solid stated synthesis; the synthesis details can be found in SI. No sign of compositional phase inhomogeneity was detected in the region of the structural phase transition within $0.45 \leq Ge/(Ge + Si) \leq 0.55$. The presence of a small amount of ZnSe as a secondary phase was detected in almost all of the samples. Only the two most Ge-rich powder samples did not show any presence of secondary phases. Additionally, Cu_xSe_y phases were detected in $Cu_{2.10}Zn_{1.04}Ge_{0.53}Si_{0.43}Se_4$ and $Cu_{1.93}Zn_{0.98}Si_{1.03}Se_4$. The Cu/(Zn + Ge + Si), Zn/(Ge + Si) and Ge/(Ge + Si) ratios of the CZGSiSe phase as well as the off-stoichiometry type[15] information and final chemical formulae of the quaternary compound, calculated according to the method described in ref. 16, are presented in Table 1.

To deepen the understanding of the phase formation, Raman spectra of $Cu_2Zn(Ge_xSi_{1-x})Se_4$ solid solutions measured under different excitation wavelengths were analyzed. Continuous changes in Raman spectra are observed with the variation of the Ge/(Ge + Si) ratio in the $Cu_2Zn(Ge_xSi_{1-x})Se_4$ solid solutions independent of the applied excitation wavelength (Fig. 2). Raman spectra of the end members of the solid solution exhibit their characteristic Raman peaks. It is noted here that in the case of $Cu_2ZnGeSe_4$ and $Cu_2ZnSiSe_4$, the measurements performed under 785 nm and 532 nm excitation wavelengths, respectively, are close to resonant conditions. This enables a more detailed analysis of the spectra of the end members. However, it also introduces additional complexity when analyzing the evolution of the Raman spectra across the entire compositional range of solid solutions. In this context, Raman measurements performed under a 442 nm excitation wavelength provide a clearer resolution of spectral variations while avoiding resonance effects, which is preferable when studying the wide compositional range of $Cu_2Zn(Ge_xSi_{1-x})Se_4$. In the case of the $Cu_2ZnGeSe_4$ compound, the corresponding peaks are seen at 177, 205, 270, and 282 cm^{-1} (peaks indicated with blue color),[17] whereas for the $Cu_2ZnSiSe_4$ compound characteristic peaks are seen at 170, 179, 211, 222, and 227 cm^{-1} (peaks indicated with green color).[18] In the case of solid solutions, mainly a two-mode behavior is observed for different peaks, which is typical of solid solutions of complex compounds.[19] Moreover, some new peaks are detected in the range 220–260 cm^{-1} (indicated with red color). One of these peaks, at 250 cm^{-1}, can be assigned to the ZnSe secondary phase, the presence of which was also detected by WDX analysis, and the 442 nm excitation wavelength is close to resonant for this compound allowing us to detect even the small concentrations of this secondary phase.[20] However, this peak is also observed in the spectra measured under 532 nm excitation (with lower relative intensity), which is not sensitive to the small amount of the ZnSe secondary phase. This suggests a more complex nature of the band at 250 cm^{-1}, where two peaks (one from ZnSe and another from $Cu_2Zn(Ge_xSi_{1-x})Se_4$ solid solution) can be overlapped. Additionally, a peak at 234 cm^{-1} cannot be assigned to any expected secondary phase (ZnSe or Cu_xSe). This suggests that both peaks at 234 and 250 cm^{-1} can be assigned to new Raman modes related to solid solution, and some of the modes

Table 1 Overview of the synthesized $Cu_2Zn(Ge_xSi_{1-x})Se_4$ solid solution: the cation ratios Cu/(Zn + Ge + Si), Zn/(Ge + Si) and Ge/(Ge + Si) of the main CZGSiSe phase obtained from the WDX analysis, chemical formula, off-stoichiometry type and presence of secondary phases

Sample name	Cu/(Zn + Ge + Si)	Zn/(Ge + Si)	Ge/(Si + Ge)	Chemical formula	Type[a] [15]	Secondary phases
Ge100 (840C)	1.04 (1)	1.12 (1)	1	$Cu_{2.09}Zn_{1.06}Ge_{0.95}Se_4$	G–F	—
Ge90Si10(840C)	1.03 (1)	1.11 (1)	0.90 (1)	$Cu_{2.07}Zn_{1.06}Ge_{0.86}Si_{0.10}Se_4$	G–F	—
Ge80Si20(840C)	1.06 (1)	1.05 (1)	0.80 (1)	$Cu_{2.10}Zn_{1.02}Ge_{0.77}Si_{0.20}Se_4$	F–I	ZnSe
Ge70Si30(840C)	1.01 (1)	1.07 (1)	0.68 (1)	$Cu_{2.03}Zn_{1.04}Ge_{0.66}Si_{0.31}Se_4$	G–F	ZnSe
Ge60Si40(840C)	1.03 (1)	1.04 (1)	0.58 (1)	$Cu_{2.06}Zn_{1.02}Ge_{0.57}Si_{0.41}Se_4$	F–I	ZnSe
Ge55Si45(840C)	1.05 (1)	1.09 (1)	0.55 (1)	$Cu_{2.10}Zn_{1.04}Ge_{0.53}Si_{0.43}Se_4$	F–I	ZnSe, CuSe, Si
Ge55Si45(900C)	1.07 (1)	1.12 (1)	0.55 (1)	$Cu_{2.13}Zn_{1.05}Ge_{0.52}Si_{0.42}Se_4$	F–I	ZnSe
Ge50Si50(840C)	1.05 (1)	1.09 (1)	0.50 (1)	$Cu_{2.10}Zn_{1.04}Ge_{0.48}Si_{0.48}Se_4$	F–I	ZnSe
Ge50Si50(900C)	1.08 (1)	1.10 (1)	0.49 (1)	$Cu_{2.14}Zn_{1.04}Ge_{0.47}Si_{0.48}Se_4$	F–I	ZnSe
Ge45Si55(840C)	1.05 (1)	1.08 (1)	0.44 (1)	$Cu_{2.10}Zn_{1.03}Ge_{0.42}Si_{0.54}Se_4$	F–I	ZnSe
Ge45Si55(900C)	1.08 (1)	1.09 (1)	0.43 (1)	$Cu_{2.14}Zn_{1.04}Ge_{0.41}Si_{0.54}Se_4$	F–I	ZnSe
Ge40Si60(900C)	0.97 (1)	0.98 (1)	0.37 (1)	$Cu_{1.95}Zn_{1.00}Ge_{0.37}Si_{0.64}Se_4$	E–J	ZnSe, CuSe
Ge30Si70(900C)	0.98 (1)	0.97 (1)	0.28 (1)	$Cu_{1.96}Zn_{0.99}Ge_{0.28}Si_{0.74}Se_4$	E–J	ZnSe, CuSe
Ge20Si80(900C)	0.95 (1)	0.95 (1)	0.17 (1)	$Cu_{1.92}Zn_{0.98}Ge_{0.18}Si_{0.85}Se_4$	E–J	ZnSe, CuSe
Ge10Si90(900C)	0.98 (1)	0.97 (1)	0.09 (1)	$Cu_{1.97}Zn_{0.98}Ge_{0.09}Si_{0.93}Se_4$	E–J	ZnSe, CuSe
Ge0(900C)	0.96 (1)	0.95 (1)	0	$Cu_{1.93}Zn_{0.98}Si_{1.03}Se_4$	E–J	Cu_2Se, ZnSe

[a] G: $Zn^{2+}_{IV} + Zn^{2+}_{I}$; F: $Cu^{+}_{IV} + Cu^{+}_{I} + Zn^{2+}_{I}$; I: $Cu^{+}_{IV} + 3Cu^{+}_{I}$; E: $2V_{Cu} + IV^{4+}_{Zn}$; J: $IV^{4+}_{Cu} + 3V_{Cu}$.

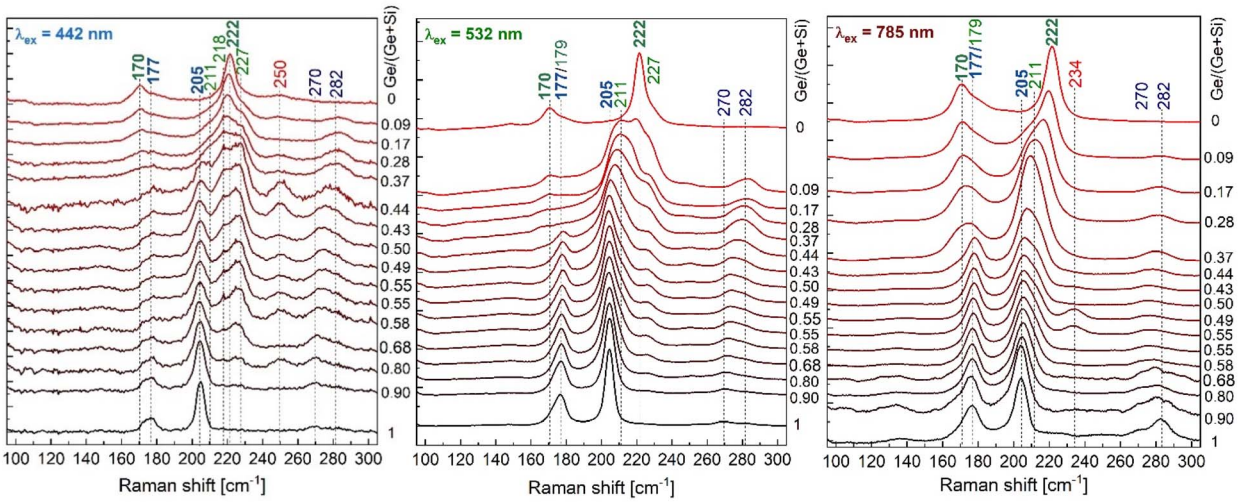

Fig. 2 Raman spectra of $Cu_2Zn(Ge_xSi_{1-x})Se_4$ solid solution measured at 442, 532 and 785 nm excitation wavelengths.

of end point compounds have a three-mode behavior. Similar behavior has been reported in the case of $Cu_2ZnSn(S,Se)_4$ solid solutions with anions substitutions,[21] but not in the case of quaternary compounds with substituted cations, which can be a specific behavior for the solid solutions with significant change of structure of the end point members.

Further analysis of the Raman peaks of the solid solution allows the detection of two specific spectral ranges where the peaks related to the end members are dominating: (1) 197–211 cm^{-1} region for the $Cu_2ZnGeSe_4$-related peaks; (2) 216–234 cm^{-1} region for the $Cu_2ZnSiSe_4$-related peaks. Calculation of the relative integrated intensity of these two spectral ranges directly shows modifications in the Raman spectra with the change of the Ge/(Ge + Si) ratio (see Fig. 3). Considering the slopes of the graph, three distinct regions can be identified, corresponding to Si-rich (Ge/(Ge + Si) ≤ 0.4) samples, Ge-rich (Ge/(Ge + Si) > 0.55) samples, as well as an intermediate region of the samples' compositional range. This leads to the assumption about different structures in the Ge- and Si-rich regions and coexistence of both kesterite and wurtz–kesterite structures in the middle compositional region, which is further developed by in-depth structural analysis.

Refinement of the crystal structure was done by a full pattern Rietveld refinement[22] using the FullProf Suite software package.[23] The kesterite type structure ($I\bar{4}$) with Cu on Wyckoff position 2*a*: (0, 0, 0) and 2*c*: $(0, \frac{1}{2}, \frac{1}{4})$, Zn on 2*d*: $(0, \frac{1}{2}, \frac{3}{4})$, Ge on 2*b*: $(\frac{1}{2}, \frac{1}{2}, 0)$ and Se on 8*g*: (*x*, *y*, *z*) was used as the structural model in the refinement of the germanium rich mixed crystals[9] and wurtz–kesterite type structure (*Pn*) with all of the cations and anions found on general positions (*x*, *y*, *z*)[10] for the silicon rich

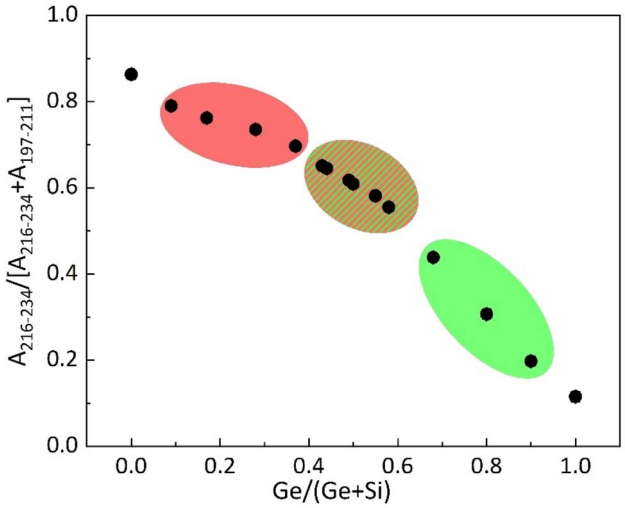

Fig. 3 Ratio between the integrated intensity of $Cu_2ZnSiSe_4$-related peaks and $Cu_2ZnGeSe_4$-related peaks as a function of the Ge/(Ge + Si) content in $Cu_2Zn(Ge_xSi_{1-x})Se_4$ solid solutions. Calculated from the Raman spectra measured under 442 nm excitation.

mixed crystals. The initial refinement of the synchrotron data used the Thompson–Cox–Hastings pseudo-Voigt algorithm for peak shape in combination with anisotropic broadening modelled by 2nd order symmetry adapted spherical harmonics, nominal composition cation occupations, neutral atomic scattering factors and isotropic Debye–Waller factors with identical values each for all selenium and metal atoms in each structure. In the monoclinic structure, the x and z positions of the (Ge, Si) cation site were kept fixed at values of 0 and 5/8, respectively, in order to avoid random drift, as the origin of these directions is not fixed by symmetry in space group *Pn*. Due to the very good counting statistics, even very minor impurities gave rise to observable Bragg peaks. These were modelled as additional phases with structure parameters taken from the ICSD or, if not identifiable, excluded from the refined data. The results of Rietveld refinement of these data can be found in the SI.

In the subsequent Rietveld refinement of the neutron diffraction data, the monoclinic angle and the cation and anion positions were fixed to the values obtained from the refinement

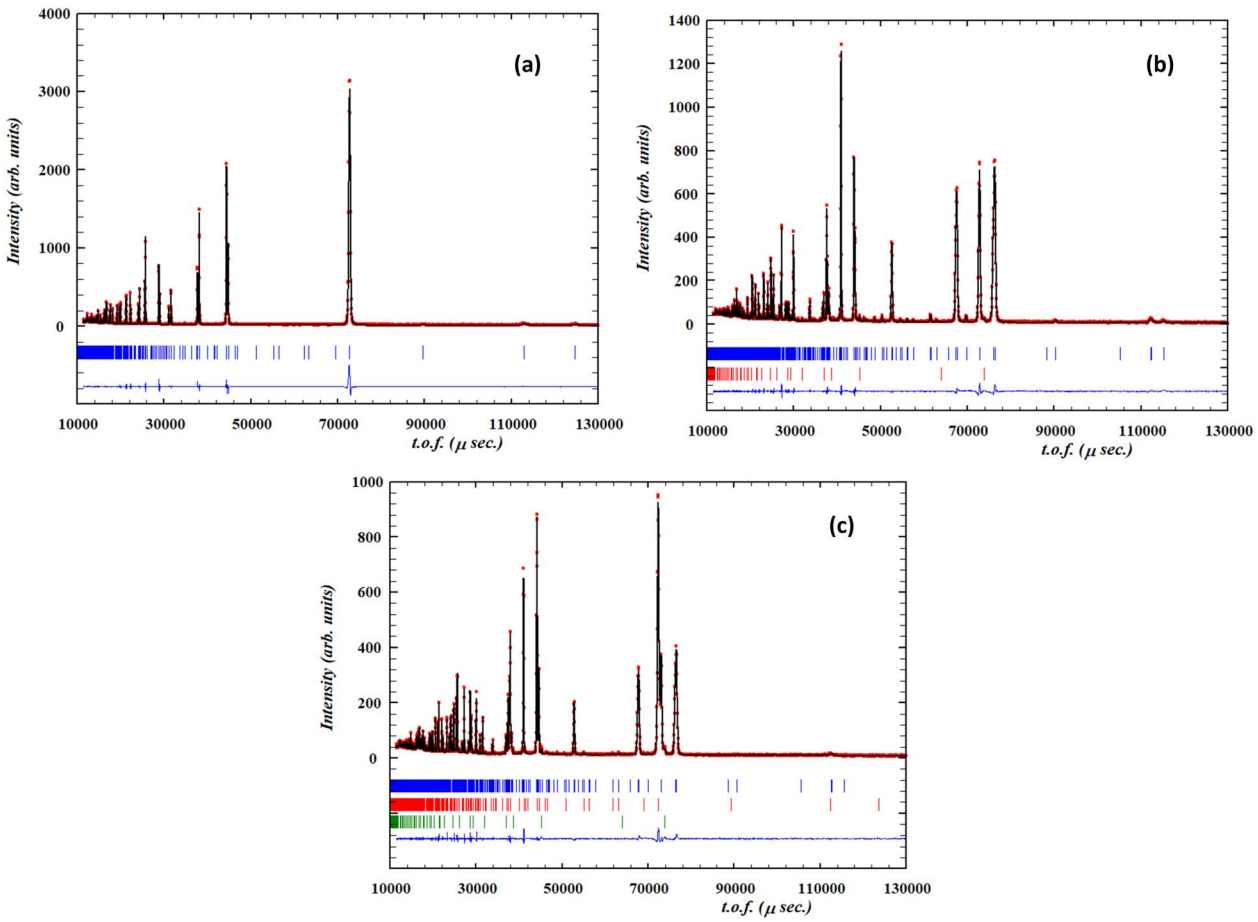

Fig. 4 Rietveld refinement against the neutron powder diffraction data of the (a) $Cu_{2.09}Zn_{1.06}Ge_{0.95}Se_4$ in space group $I\bar{4}$. The red dots are experimental data, the black line is the obtained fit, the blue ticks are the Bragg peak positions of the kesterite type structure, and the blue line is the difference between the experimental and calculated intensities; (b) $Cu_{1.93}Zn_{0.98}Si_{1.03}Se_4$ in space group *Pn*. The red dots are experimental data, the black line is the obtained fit, the blue ticks are the Bragg peak positions of the wurtz–kesterite type structure, the red ticks are the Bragg peak positions of the ZnSe secondary phase and the blue line is the difference between the experimental and calculated intensities; (c) $Cu_{2.10}Zn_{1.03}Ge_{0.42}Si_{0.54}Se_4$ where the red dots are experimental data, the black line is the obtained fit, the blue ticks are the Bragg peak positions of the kesterite-type structure (space group $I\bar{4}$), the red ticks are the Bragg peak positions of the wurtz–kesterite-type structure (space group *Pn*), the green ticks are the Bragg peak positions of the ZnSe secondary phase and the blue line is the difference between the experimental and calculated intensities.

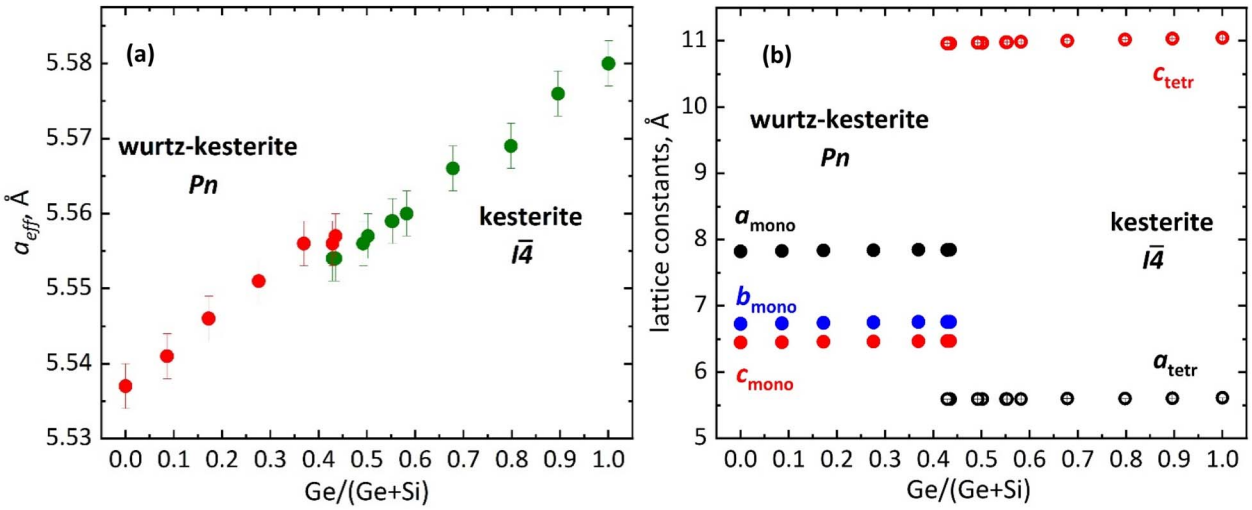

Fig. 5 (a) Effective lattice parameter a_{eff}, (b) lattice parameters a, b and c, of the $Cu_2Zn(Ge_xSi_{1-x})Se_4$ mixed crystals of the tetragonal kesterite type structure and the monoclinic wurtz–kesterite type structure with dependence on the cation ratio Ge/(Ge + Si).

of synchrotron X-ray diffraction data. The refinement of site occupancy factors (SOFs) was done without any chemical constraints. Three neutron powder diffraction patterns and the corresponding Rietveld analysis are shown exemplarily (see Fig. 4) for the end members $Cu_2ZnGeSe_4$ (applying the kesterite-type structure) and $Cu_2ZnSiSe_4$ (applying the wurtz–kesterite-type structure) as well as a $Cu_2ZnGe_xSi_{1-x}Se_4$ mixed crystal with Ge/(Ge + Si) = 0.45 where both structure types were applied. For the latter, it can be clearly seen in the diffractogram (Fig. 4c) that Bragg peaks attributed to both kesterite and wurtz–kesterite structures are present. For mixed crystals in the $0.45 \leq$ Ge/(Ge + Si) ≤ 0.55 region, both the tetragonal and monoclinic structures were refined. Thus, it was concluded that in the compositional region of the structural phase transition mixed crystals with the same chemical composition but different crystal structure, either the kesterite or the wurtz–kesterite structure coexist.

The lattice parameters, determined by Rietveld analysis of the diffraction data, follow Vegard's law[24] for both structural regions. In order to follow the lattice constant parameter development through the whole series, the effective lattice parameter a_{eff}, adapted from ref. 1, was calculated according to eqn (1) (see Fig. 5a).

$$a_{\mathrm{eff\ tetr}} = \sqrt[3]{(a_{\mathrm{tetr}}{}^2 c_{\mathrm{t}})/2}$$
$$a_{\mathrm{eff\ mono}} = \sqrt[3]{(a_{\mathrm{mono}} b_{\mathrm{mono}} c_{\mathrm{mono}})/2} \quad (1)$$

The steady, linear increase of a_{eff} suggests that mixed crystals in the $0.45 \leq$ Ge/(Ge + Si) ≤ 0.55 region have indeed a homogeneous chemical composition, while two structural phases are present simultaneously.[7]

The lattice parameter for the end members and the mixed crystals of the $Cu_2Zn(Ge_xSi_{1-x})Se_4$ series are presented in

Table 2 Lattice parameters of the monoclinic wurtz–kesterite type structure and tetragonal kesterite type structure as well as a_{eff} obtained from the refinement of neutron diffraction data

Sample name	a_{tetr}, Å	c_{tetr}, Å	a_{mono}, Å	b_{mono}, Å	c_{mono}, Å	β_{mono}, °	$a_{eff\ tetr}$, Å	$a_{eff\ mono}$, Å
Ge100(840C)	5.610 (1)	11.043 (2)					5.580 (3)	
Ge90Si10(840C)	5.606 (1)	11.031 (2)					5.576 (3)	
Ge80Si20(840C)	5.599 (1)	11.017 (2)					5.569 (3)	
Ge70Si30(840C)	5.600 (1)	10.999 (2)					5.566 (3)	
Ge60Si40(840C)	5.595 (1)	10.983 (2)					5.560 (3)	
Ge55Si45(840C)	5.595 (1)	10.975 (2)					5.559 (3)	
Ge55Si45(900C)	5.595 (1)	10.976 (2)					5.559 (3)	
Ge50Si50(840C)	5.594 (1)	10.967 (2)					5.557 (3)	
Ge50Si50(900C)	5.593 (1)	10.968 (2)					5.556 (3)	
Ge45Si55(840C)	5.592 (1)	10.959 (2)	7.846 (1)	6.759 (1)	6.471 (1)	90.0160 (1)	5.554 (3)	5.557 (3)
Ge45Si55(900C)	5.592 (1)	10.959 (2)	7.845 (1)	6.758 (1)	6.470 (1)	90.0131 (1)	5.554 (3)	5.556 (3)
Ge40Si60(900C)			7.847 (1)	6.757 (1)	6.469 (1)	90.0167 (1)		5.556 (3)
Ge30Si70(900C)			7.840 (1)	6.750 (1)	6.464 (1)	90.0179 (1)		5.551 (3)
Ge20Si80(900C)			7.835 (1)	6.743 (1)	6.459 (1)	90.0256 (1)		5.546 (3)
Ge10Si90(900C)			7.828 (1)	6.736 (1)	6.454 (1)	90.0473 (1)		5.541 (3)
Ge0(900C)			7.822 (1)	6.730 (1)	6.450 (1)	90.0593 (1)		5.537 (3)

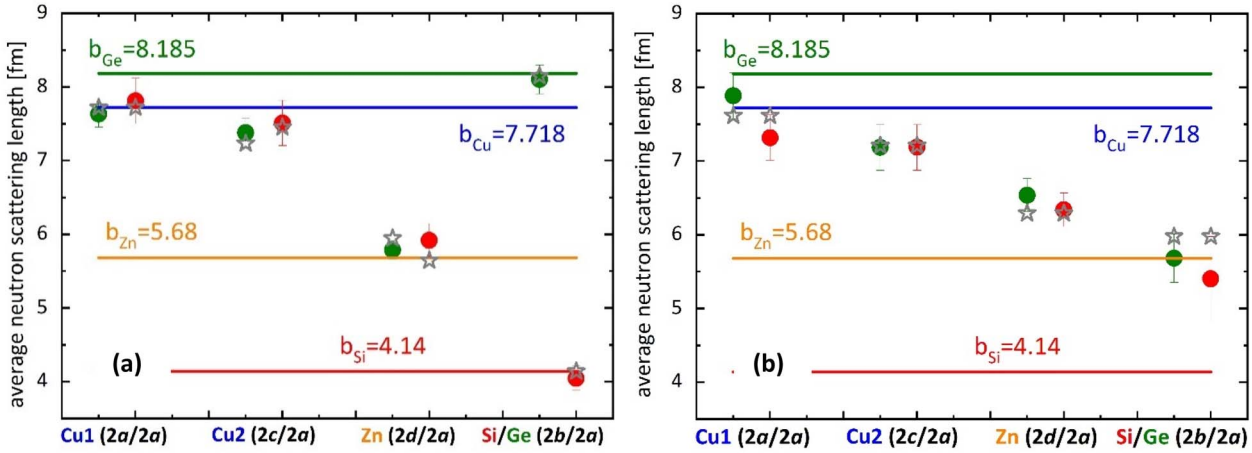

Fig. 6 (a) Average neutron scattering length $\bar{b}$ of the cation sites 2*a*, 2*c*, 2*d* and 2*b*, assuming a kesterite type structure exemplarily shown for a tetragonal mixed crystal, $Cu_{2.09}Zn_{1.06}Ge_{0.95}Se_4$ (green dots) in comparison to the average neutron scattering length $\bar{b}$ of the four 2*a* cation sites assuming the wurtz–kesterite type structure exemplarily shown for a monoclinic mixed crystal, $Cu_{1.93}Zn_{0.98}Si_{1.03}Se_4$ (red dots). Full symbols – experimental average neutron scattering length, stars – calculated average neutron scattering length according to a cation distribution model. (b) The comparison of two cation distributions within a mixed crystal in the structural transition region, $Cu_{2.10}Zn_{1.03}Ge_{0.42}Si_{0.54}Se_4$, containing two structural phases (kesterite and wurtz–kesterite) with the same chemical compositions (the symbol designations are the same as in (a)).

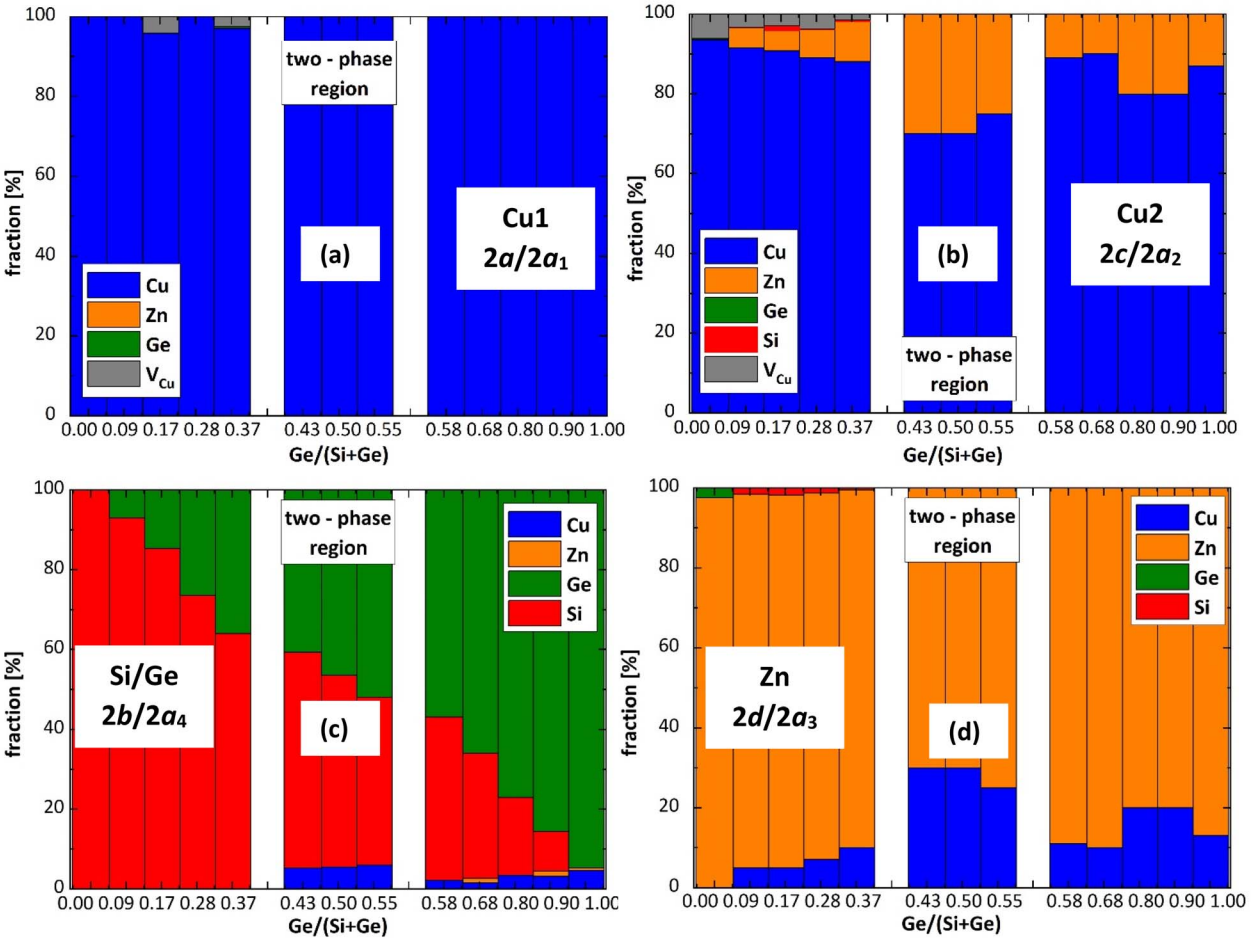

Fig. 7 The resulting cation distribution on the structural sites (a) $2a/2a_1$, (b) $2c/2a_2$, (c) $2b/2a_4$ and (d) $2d/2a_3$ of kesterite and wurtz–kesterite structures for the whole $Cu_2Zn(Ge_xSi_{1-x})Se_4$ solid solution, obtained from the in-depth analysis of neutron diffraction data. Within the columns for one Wyckoff site the Ge-content increases from left to right.

Table 3 The cation distribution model for each of the mixed crystals from the $Cu_2Zn(Ge_xSi_{1-x})Se_4$ solid solution (*V* indicates vacancies)

	$2a/2a_1$		$2c/2a_2$			$2d/2a_3$				$2b/2a_4$				Interstitials	
Sample name	*V*	Cu	*V*	Cu	Zn	Cu	Zn	Ge	Si	Cu	Zn	Ge	Si	Cu_i	Zn_i
Ge100(840C)		1.00		0.87	0.13	0.13	0.87			0.05		0.95		0.05	0.05
Ge90Si10(840C)		1.00		0.80	0.20	0.20	0.80			0.03	0.01	0.86	0.10	0.03	0.05
Ge80Si20(840C)		1.00		0.80	0.20	0.20	0.80			0.03		0.77	0.20	0.07	0.02
Ge70Si30(840C)		1.00		0.90	0.10	0.10	0.90			0.02	0.01	0.66	0.31	0.02	0.03
Ge60Si40(840C)		1.00		0.89	0.11	0.11	0.89			0.02		0.57	0.41	0.03	0.02
Ge55Si45(840C)		1.00		0.75	0.25	0.25	0.75			0.06		0.52	0.42	0.06	0.04
Ge55Si45(900C)		1.00		0.75	0.25	0.25	0.75			0.06		0.52	0.42	0.08	0.05
Ge50Si50(840C)	0.05	0.95		0.70	0.30	0.30	0.70			0.06		0.47	0.48	0.06	0.04
Ge50Si50(900C)	0.05	0.95		0.70	0.30	0.30	0.70			0.06		0.47	0.48	0.09	0.04
Ge45Si55(840C)		1.00		0.70	0.30	0.30	0.70			0.05		0.42	0.54	0.06	0.03
Ge45Si55(900C)		1.00		0.70	0.30	0.30	0.70			0.05		0.42	0.54	0.09	0.04
Ge40Si60(900C)	0.03	0.97	0.01	0.88	0.11	0.10	0.90					0.36	0.64		
Ge30Si70(900C)		1.00	0.04	0.89	0.07	0.07	0.92	0.01				0.26	0.74		
Ge20Si80(900C)	0.04	0.96	0.03	0.91	0.05	0.05	0.93	0.02				0.15	0.85		
Ge10Si90(900C)		1.00	0.03	0.92	0.05	0.05	0.93	0.02				0.07	0.93		
Ge0(900C)		1.00	0.06	0.94			0.98		0.02				1.00		

Table 4 Concentration of deduced cation point defects $[cm^{-3}] \times 10^{20}$

Sample name	Cu_{IV}	err+	err−	Zn_{IV}	err+	err−	Cu_I	err	Zn_i	err	Cu/Zn disorder	err
Ge100(840C)	1.352	0.201	0.317	0.201	0.029	0.201	1.324	0.029	1.525	0.029	3.740	0.471
Ge90Si10(840C)	0.923	0.346	0.029	0.375	0.144	0.375	0.923	0.029	1.298	0.029	5.769	0.169
Ge80Si20(840C)	0.984	0.434	0.087				1.969	0.029	0.463	0.029	5.790	0.751
Ge70Si30(840C)	0.464	0.232	0.029	0.319	0.157	0.319	0.435	0.029	0.783	0.029	2.899	0.657
Ge60Si40(840C)	0.640	0.349	0.029				0.960	0.029	0.465	0.029	3.199	0.816
Ge55Si45(840C)	1.368	0.524	0.378				1.688	0.029	1.222	0.029	7.276	0.632
Ge55Si45(900C)	1.746	0.262	0.143				2.241	0.058	1.455	0.029	7.276	1.996
Ge50Si50(840C)	1.399	0.029	0.903				1.865	0.029	1.195	0.029	8.741	1.253
Ge50Si50(900C)	1.603	0.029	0.105				2.507	0.058	1.137	0.029	8.743	1.984
Ge45Si55(840C)	1.226	0.029	0.759				1.838	0.029	0.963	0.029	8.754	1.084
Ge45Si55(900C)	1.546	0.029	0.963				2.509	0.058	0.929	0.029	8.753	1.392

Sample name	V_{Cu}	err	IV_{Zn}	err+	err−	IV_{Cu}	err+	err−	Cu/Zn disorder	err
Ge40Si60(900C)	0.979	0.477	0.126	0.025	0.025	0.126	0.025	0.050	2.510	0.253
Ge30Si70(900C)	0.931	0.252	0.327	0.101	0.050	0.076	0.025	0.025	1.761	0.344
Ge20Si90(900C)	1.816	0.555	0.454	0.252	0.025	0.303	0.076	0.010	1.261	0.423
Ge10Si90(900C)	0.834	0.177	0.405	0.126	0.051	0.025	0.003	0.003	1.264	0.391
Ge0(900C)	1.546	0.912	0.633	0.329	0.025	0.101	0.051	0.025	0	0

Table 2 and Fig. 5b. The details of the refinement can be found in the SI.

The average neutron scattering length analysis method[25] was applied to determine the distribution of the cations Cu^+, Zn^{2+} Ge^{4+} and Si^{4+} on the four structural sites of the kesterite and wurtz–kesterite type structures. The experimental average neutron scattering lengths (b) of the cation structural sites were calculated according to eqn (2) for the kesterite type structure and eqn (3) for the wurtz–kesterite type structure using the cation site occupancy factors SOF_{2a}, SOF_{2b}, SOF_{2c} and SOF_{2d} as well as SOF_{2a_1}, SOF_{2a_2}, SOF_{2a_3} and SOF_{2a_4} determined by Rietveld analysis of neutron diffraction data.

$$\begin{aligned} \overline{b}_{2a}(\exp) &= \mathrm{SOF}_{2a} \cdot b_{\mathrm{Cu}} \\ \overline{b}_{2c}(\exp) &= \mathrm{SOF}_{2c} \cdot b_{\mathrm{Cu}} \\ \overline{b}_{2d}(\exp) &= \mathrm{SOF}_{2d} \cdot b_{\mathrm{Zn}} \\ \overline{b}_{2b}(\exp) &= \mathrm{SOF}_{2b} \cdot b_{\mathrm{Ge}} \end{aligned} \quad (2)$$

$$\begin{aligned} \overline{b}_{2a_1}(\exp) &= \mathrm{SOF}_{2a_1} \cdot b_{\mathrm{Cu}} \\ \overline{b}_{2a_2}(\exp) &= \mathrm{SOF}_{2a_2} \cdot b_{\mathrm{Cu}} \\ \overline{b}_{2a_3}(\exp) &= \mathrm{SOF}_{2a_3} \cdot b_{\mathrm{Zn}} \\ \overline{b}_{2a_4}(\exp) &= \mathrm{SOF}_{2a_4} \cdot b_{\mathrm{Si}} \end{aligned} \quad (3)$$

The calculated average neutron scattering length is derived from a cation distribution model taking into account the

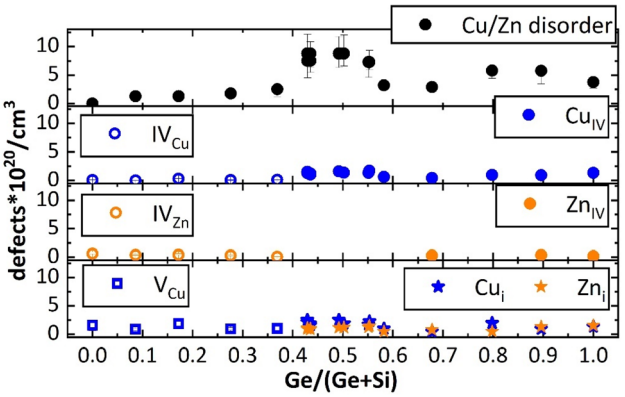

Fig. 8 Concentration of Cu_{Zn} and Zn_{Cu} anti site defects (defects per cm^3) representing Cu/Zn disorder (black dots) as well as the off-stoichiometry related defects Cu_{IV} (blue dots), VI_{Cu} (empty blue dots), Zn_{IV} (orange dots), IV_{Zn} (empty orange dots), V_{Cu} (empty blue squares), Cu_i (blue stars) and Zn_i (orange stars).

experimentally determined total amounts of each element, as obtained by WDX analysis, and assuming that all four cation sites are fully occupied. A comparison of the experimental and calculated average neutron scattering length is shown in Fig. 6. The presence of intrinsic point defects is included in the cation distribution model. For example, the decrease of the average neutron scattering length of the Cu site $2a$ in the kesterite type or $2a_1$ in the wurtz–kesterite type structure indicates the presence of a less scattering species on that structural site, such as a copper vacancy (V_{Cu}) or the anti-site defect Zn_{Cu}. On the other hand, the increase of the average scattering length on the Zinc site $2d$ or $2a_3$ site in the kesterite or wurtz–kesterite structure, respectively, would indicate the presence of a species scattering more, *e.g.* Cu or Ge forming an anti-site. It is important that the sum of a cation species on the different cation sites is in good agreement with the chemical composition of the phase determined by WDX analysis. The resulting cation distributions for all the mixed crystals in the $Cu_2Zn(Ge_xSi_{1-x})Se_4$ series are presented in Fig. 7. The detailed cation distribution model is presented in Table 3. The results for the end member $Cu_2ZnGeSe_4$ are in agreement to ref. 9 and those for the other end member $Cu_2ZnSiSe_4$ are in agreement with ref. 10. In the $Cu_2Zn(Ge_xSi_{1-x})Se_4$ mixed crystals, both Si and Ge are randomly distributed on the $2b/2a_4$ sites of the kesterite/wurtz–kesterite structure also across the structural transition. In the Cu-rich mixed crystals with $0.58 \leq Ge/(Ge + Si) \leq 1$, there is a small amount of copper on these sites forming anti-sites Cu_{Ge} and Cu_{Si}, respectively, corresponding to the off-stoichiometry type scenario.[15] The $2a/2a_1$ site is occupied by Cu in agreement with the kesterite and wurtz–kesterite crystal structure definition, with a small presence of V_{Cu} in Cu-poor mixed crystals, which is also in a very good agreement with the off-stoichiometry type scenario.[15] Additionally, copper and zinc interstitials (Cu_i and Zn_i) are

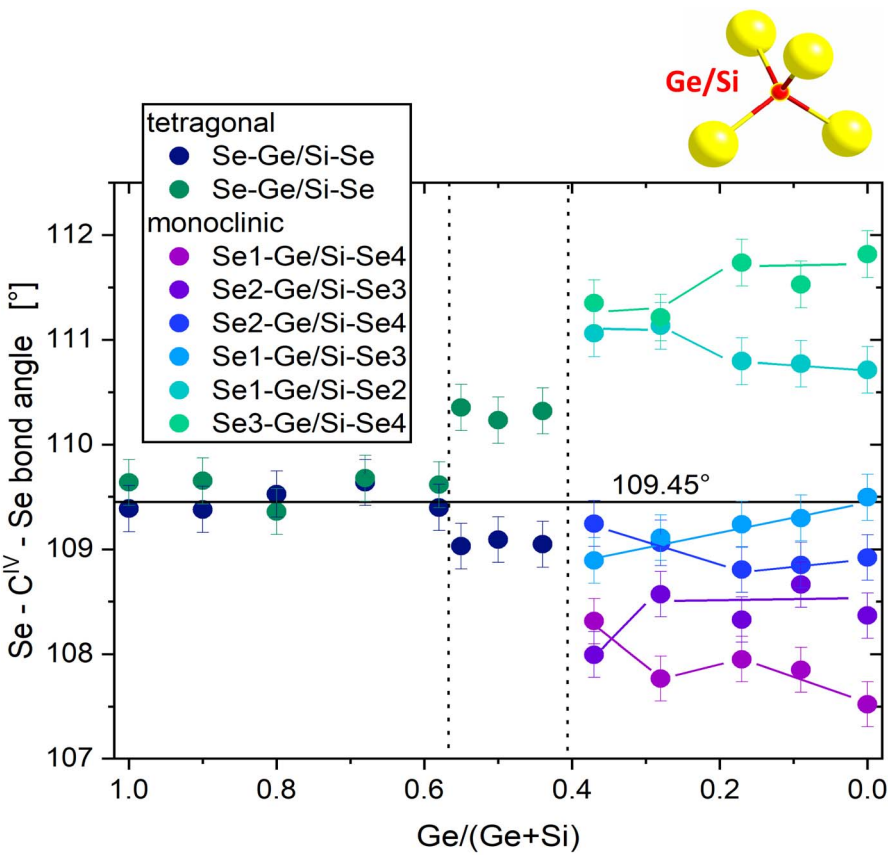

Fig. 9 Deviations from ideal bond angle (absolute values) in the anion tetrahedron around the four-valent cation (Ge and Si) with dependence on the Ge/(Ge + Si) ratio.

Table 5 Optical band gap energy of $Cu_2Zn(Ge_xSi_{1-x})Se_4$ mixed crystals obtained from diffuse reflectance

Sample name	E_g, eV
Ge100(840C)	1.31 (5)
Ge90Si10(840C)	1.36 (5)
Ge80Si20(840C)	1.41 (5)
Ge70Si30(840C)	1.47 (5)
Ge60Si40(840C)	1.54 (5)
Ge55Si45(840C)	1.56 (5)
Ge55Si45(900C)	1.57 (5)
Ge50Si50(840C)	1.62 (5)
Ge50Si50(900C)	1.61 (5)
Ge45Si55(840C)	1.70 (5)
Ge45Si55(900C)	1.71 (5)
Ge40Si60(900C)	1.78 (5)
Ge30Si70(900C)	1.86 (5)
Ge20Si80(900C)	1.95 (5)
Ge10Si90(900C)	2.04 (5)
Ge0(900C)	2.22 (5)

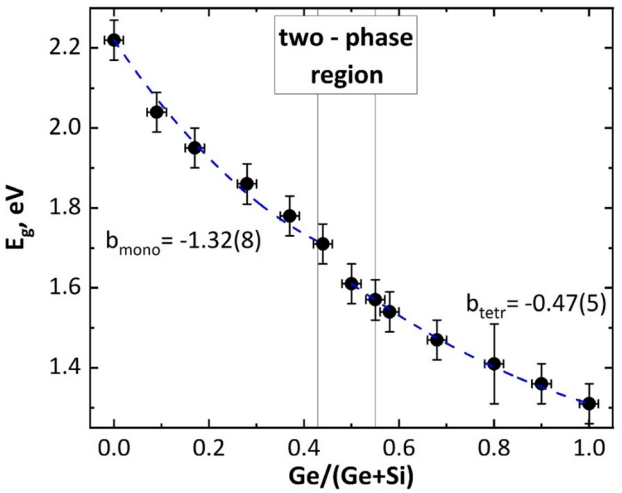

Fig. 10 Band gap energies of the $Cu_2Zn(Ge_xSi_{1-x})Se_4$ solid solution with dependence on the cation ratio Ge/(Ge + Si).

present in Cu-rich and Zn-rich mixed crystals. It can be summarized that all the off-stoichiometry related point defects found experimentally (see Table 4 and Fig. 8) are in agreement with the off-stoichiometry type model[15] and were found to not be influenced by the structural phase transition.

The 2*c* and 2*d* sites of the kesterite type structure in Ge-rich mixed crystals show a very typical picture, where equal amounts of Cu_{Zn} and Zn_{Cu} anti-site defects are present – the Cu/Zn disorder,[4] which is often observed in kesterite-type Ge-containing quaternary chalcogenides.[9] On the other hand, wurtz–kesterite type $Cu_2ZnSiSe_4$, with an off-stoichiometric composition $Cu_{1.93}Zn_{0.98}Si_{1.03}Se_4$ does not show any presence of Cu/Zn disorder, which is in good agreement with a previously published MEAD study.[10] With the increasing amount of Ge in $Cu_2Zn(Ge_xSi_{1-x})Se_4$ mixed crystals though, we see the appearance and increase of Cu/Zn disorder even in the wurtz–kesterite type structure (Cu_{Zn} and Zn_{Cu} on the sites $2a_2$ and $2a_3$). Interestingly enough, it was possible to describe the cation distribution in both structural phases (kesterite and wurtz–kesterite) within the two-phase region of the same sample with the same distribution of the cations on the corresponding sites (see Fig. 6b). In this case, the Cu/Zn disorder was the strongest, with the fraction of Cu_{Zn} on $2d/2a_3$ and Zn_{Cu} on $2c/2a_2$ reaching as high as 0.3 (see Table 3 and Fig. 8).

It is suggested that the structural phase transition from the kesterite type to the wurtz–kesterite type structure occurs *via* the co-existence of two types of domains, tetragonal and monoclinic ones, with the same chemical composition, composed of the same building blocks – anion/cation tetrahedra which are differently distorted, in this way making it a distortion driven transition. This distortion becomes visible in the bond angles within the $IVSe_4$ tetrahedron (IV stands for the four-valent cation), see Fig. 9. The deviation of the Se–Ge–Se bond angles from the bond angle in an ideal (regular) tetrahedron (109.45°) is small in the case of $Cu_2ZnGeSe_4$ and the tetragonal mixed crystals but increases in the tetragonal phase of the 2-phase region. On the other hand, the $SiSe_4$ coordination tetrahedron is heavily distorted resulting in six different Se–Si–Se bond angles in $Cu_2ZnSiSe_4$.

In order to correlate the structural changes as well as the obtained point defect concentrations with the optoelectronic properties of these materials, the optical band gap energy E_g was determined by diffuse reflectance spectroscopy (DRS). Tauc plots were obtained by plotting $(F(R) \times h\nu)^2$ *versus* the photon energy,[26] and the linear part of the curve was extrapolated to the baseline, and the optical band gap was extracted from the value of intersection (Fig. S1 in the SI). An estimation of the band gap energy in the same way was previously reported for Cu_2ZnSnS_4 (CZTS), $Cu_2ZnSnSe_4$ (CZTSe) and $Cu_2ZnGeSe_4$ (CZGSe) powder samples,[11] proving the applicability of this approach. It is found that the band gap energy E_g within the $Cu_2Zn(Ge_xSi_{1-x})Se_4$ series is changing in the range of 1.31 eV to 2.22 eV. The obtained E_g values can be found in Table 5 and Fig. 10. Both Ge-rich tetragonal and Si-rich monoclinic parts of the solid solution show a bowing behaviour according to eqn (4), typically observed in compound semiconductors.[11]

$$E_g(x) = E_g^{x=0}\cdot(1-x) + E_g^{x=1}\cdot x + b(1-x)x \text{ with } x = \text{Ge}/(\text{Ge}+\text{Si}) \quad (4)$$

The bowing parameter b was determined to be $b = -1.32$ for Si-rich monoclinic mixed crystals and $b = -0.48$ for Ge-rich tetragonal mixed crystals, respectively. This is in a very good agreement with the fact that Vegard's law is followed in solid solutions only as long as the structure does not change. Thus, with two different bowing parameters for two different structures, two solid solutions were derived. In the region of interest for the tandem applications, the band gap of 1.6–1.8 eV (ref. 27) is also achieved within the investigated series. It partially overlaps with the two-phase region, which could have potential consequences for the efficiency of the fabricated devices.

The results of this study highlight the importance of considering alternative materials beyond the known

chalcopyrites (Cu(In,Ga)Se_2) or kesterites in the search for low-cost and environmentally friendly top absorber layers and demonstrate that cation mutation in quaternary chalcogenides is a promising path towards the development of highly efficient tandem solar cells.

4. Conclusion

Neutron and X-ray synchrotron powder diffraction, wavelength dispersive X-ray spectroscopy, and Raman and diffuse reflectance spectroscopy were used to investigate the structural phase transition in the $Cu_2Zn(Ge_xSi_{1-x})Se_4$ series of powder samples. These studies showed that Si-rich mixed crystals with Ge/(Ge + Si) = 0–0.37 adopt the monoclinic wurtz–kesterite type structure (space group *Pn*), whereas Ge-rich mixed crystals with Ge/(Ge + Si) = 0.59–1.0 crystallize in the tetragonal kesterite type structure (space group $I\bar{4}$). In $Cu_2Zn(Ge_xSi_{1-x})Se_4$ mixed crystals with Ge/(Ge + Si) = 0.45–0.55, two phases with the same chemical composition but different crystal structure co-exist. The IV-valent cations (Si^{4+} an Ge^{4+}) are randomly distributed on the same structural site (in both structure types) through the whole $Cu_2Zn(Ge_xSi_{1-x})Se_4$. The off-stoichiometry type related intrinsic point defect scenario is not influenced by the phase transition. The structural phase transition occurs in the following way: the cations shift from special positions (in the kesterite type structure) to more general positions (in the wurtz–kesterite type structure). The distortion of the anion (and cation) tetrahedra increases, which results in a symmetry reduction, making it a distortion driven transition. The band gap range of 1.31 eV to 2.22 eV can be covered by the samples from $Cu_2Zn(Ge_xSi_{1-x})Se_4$ series, which makes it promising for tandem applications.

Conflicts of interest

There are no conflicts of interest to declare.

Data availability

All data supporting the findings of this study are available in the SI associated with this manuscript. See DOI: https://doi.org/10.1039/d5ta06163f.

Acknowledgements

A portion of this research used resources at the Spallation Neutron Source, a DOE Office of Science User Facility operated by the ORNL within the IPTS 29192.1. We acknowledge the HZDR BM20 ROBL station at ESRF for providing beamtime within the proposal A20-1-822. The research leading to the results presented has been partially supported by the INFINITE-CELL project. This project has received funding from the European Union's Horizon 2020 research and innovation programme under the Marie Skłodowska-Curie grant agreement no. 777968. The authors from IREC are grateful for the financial support of MCIN/AEI/10.13039/501100011033 and co-finance of the European Union through the projects HIDDEN-PV (PCI2023-143430), belong to the MNT-Solar Consolidated Research Group of the "Generalitat de Catalunya" (ref. 2021 SGR 01286) and are grateful to European Regional Development Funds (ERDF, FEDER Programa Competitivitat de Catalunya 2007–2013). V. R. acknowledges the support of the predoctoral program AGAUR-FI ajuts (2023 FI-1 00436) Joan Oro of the Secretariat of Universities and Research of the Department of Research and Universities of the Generalitat of Catalonia and the European Social Plus Fund. M. G. acknowledges the financial support from MCIN/AEI/10.13039/501100011033 and from FSE+ in the framework of Ramon y Cajal fellowship (RYC2022-035588-I). This article is partially based upon the work from COST Action ReNewPV CA21148, supported by COST (European Cooperation in Science and Technology).

References

1 S. Adachi, *Earth-abundant materials for solar cells: Cu_2-II-IV-VI_4 semiconductors*, John Wiley & Sons, 2015, DOI: 10.1002/9781119052814.
2 NREL chart, https://www.nrel.gov/pv/cell-efficiency.html.
3 J. Zhou, X. Xu, B. Duan, H. Wu, J. Shi, Y. Luo, D. Li and Q. Meng, Regulating crystal growth via organic lithium salt additive for efficient kesterite solar cells, *Nano Energy*, 2021, **89B**, 106405, DOI: 10.1016/j.nanoen.2021.106405.
4 S. Schorr, H.-J. Höbler and M. Tovar, A neutron diffraction study of the stannite-kesterite solid solution series, *Eur. J. Mineral.*, 2007, **19**, 65–73, DOI: 10.1127/0935-1221/2007/0019-0065.
5 X. Liu, Y. Feng, H. Cui, F. Liu, X. Hao, G. Conibeer, D. B. Mitzi and M. Green, The current status and future prospects of kesterite solar cells: a brief review, *Progress in Photovoltaics: Research and Applications*, 2016, **24**, 879–898, DOI: 10.1002/pip.2741.
6 G. Gurieva, J. A. Marquez, A. Franz, C. J. Hages, S. Levcenko, T. Unold and S. Schorr, Effect of Ag incorporation on structure and optoelectronic properties of $(Ag_{1-x}Cu_x)_2ZnSnSe_4$ solid solutions, *Phys. Rev. Mater.*, 2020, **4**, 054602, DOI: 10.1103/physrevmaterials.4.054602.
7 S. Schorr, The crystal structure of kesterite type compounds: a neutron and X-ray diffraction study, *Sol. Energy Mater. Sol. Cells*, 2011, **95**, 1482, DOI: 10.1016/j.solmat.2011.01.002.
8 G. Gurieva, S. Niedenzu, N. Siminel, A. Franz and S. Schorr, The kesterite–stannite structural transition as a way to avoid Cu/Zn disorder in kesterites: the exemplary case of the $Cu_2(Zn,Mn)SnSe_4$, *Faraday Discuss.*, 2022, **239**, 51–69, DOI: 10.1039/D2FD00042C.
9 G. Gurieva, D. M. Többens, M. Y. Valakh and S. Schorr, Cu-Zn disorder in $Cu_2ZnGeSe_4$: a complementary neutron diffraction and Raman spectroscopy study, *J. Phys. Chem. Solids*, 2016, **99**, 100–104, DOI: 10.1016/j.jpcs.2016.08.017.
10 D. M. Többens, G. Gurieva, S. Niedenzu, G. Schuck, I. Zizak and S. Schorr, Cation distribution in $Cu_2ZnSnSe_4$, Cu_2FeSnS_4 and $Cu_2ZnSiSe_4$ by multiple-edge anomalous diffraction, *Struct. Sci.*, 2020, **76**(6), 1027–1035, DOI: 10.1107/S2052520620013384.
11 S. Schorr and G. Gurieva, Energy band gap variations in chalcogenide compound semiconductors: influence of

crystal structure, structural disorder, and compositional variations, in *Crystallography in Materials Science: From Structure-Property Relationships to Engineering*, ed. S. Schorr and C. Weidenthaler, Walter de Gruyter GmbH, Berlin, Munich, Boston, 2021, pp. 123–151, DOI: 10.1515/9783110674910-004.

12 S. Niedenzu, G. Gurieva and S. Schorr, Challenges and structural characterization of the solid solution $Cu_2Zn(Ge_xSi_{1-x})Se_4$, in *2018 IEEE 7th World Conference on Photovoltaic Energy Conversion (WCPEC) (A Joint Conference of 45th IEEE PVSC, 28th PVSEC & 34th EU PVSEC)*, IEEE, 2018, pp. 3290–3293, DOI: 10.1109/PVSC.2018.8547352.

13 A. C. Scheinost, J. Claussner, J. Exner, M. Feig, S. Findeisen, C. Hennig, K. O. Kvashnina, D. Naudet, D. Prieur, A. Rossberg and M. Schmidt, ROBL-II at ESRF: a synchrotron toolbox for actinide research, *Synchrotron Radiat.*, 2021, **28**(1), 333–349, DOI: 10.1107/S1600577520014265.

14 A. Huq, M. J. Kirkham, P. F. Peterson, J. P. Hodges, P. Whitfield, K. Page, T. Huegle, E. B. Iverson and A. Parizzi, Rennich G Q POWGEN: rebuild of a third-generation powder diffractometer at the Spallation Neutron Source, *J. Appl. Crystallogr.*, 2019, **52**, 1189–1201, DOI: 10.1107/S160057671901121X.

15 S. Schorr, G. Gurieva, M. Guc, M. Dimitievska, A. Perez-Rodriguez, V. Izquierdo-Roca, C. Schnohr, J. Kim, W. Jo and J. M. Merino, Point defects, compositional fluctuations, secondary phases in non-stoichiometric kesterites, *JPhys Energy*, 2020, **2**, 012002, DOI: 10.1088/2515-7655/ab4a25/.

16 G. Gurieva, L. E. Valle Rios, A. Franz, P. Whitfield and S. Schorr, Intrinsic point defects in off-stoichiometric $Cu_2ZnSnSe_4$: a neutron diffraction study, *J. Appl. Phys.*, 2018, **123**, 161519, DOI: 10.1063/1.4997402.

17 M. Guc, S. Levcenko, V. Izquierdo-Roca, X. Fontané, E. Arushanov and A. Pérez-Rodríguez, Polarized Raman scattering analysis of $Cu_2ZnSnSe_4$ and $Cu_2ZnGeSe_4$ single crystals, *J. Appl. Phys.*, 2013, **114**(19), 193514, DOI: 10.1063/1.4830028.

18 M. Guc, S. Levcenko, V. Izquierdo-Roca, X. Fontane, M. Ya. Valakh, E. Arushanov and A. Pérez-Rodríguez, Polarized Raman scattering analysis of Cu_2ZnSiS_4 and $Cu_2ZnSiSe_4$ single crystals, *J. Appl. Phys.*, 2013, **114**(17), 173507, DOI: 10.1063/1.4828885.

19 E. Garcia-Llamas, M. Guc, I. V. Bodnar, X. Fontané, R. Caballero, J. M. Merino and V. Izquierdo-Roca, Multiwavelength excitation Raman scattering of $Cu_2ZnSn_{1-x}Ge_x(S,Se)_4$ single crystals for earth abundant photovoltaic applications, *J. Alloys Compd.*, 2017, **692**, 249–256, DOI: 10.1016/j.jallcom.2016.09.035.

20 M. Dimitrievska, H. Xie, A. J. Jackson, X. Fontané, M. Espíndola-Rodríguez, E. Saucedo and V. Izquierdo-Roca, Resonant Raman scattering of ZnS_xSe_{1-x} solid solutions: the role of S and Se electronic states, *Phys. Chem. Chem. Phys.*, 2016, **18**(11), 7632–7640, DOI: 10.1039/C5CP04498G.

21 M. Dimitrievska, H. Xie, A. Fairbrother, X. Fontané, E. Saucedo, V. Izquierdo-Roca, G. Gurieva, A. Pérez-Rodríguez and S. Schorr, Multiwavelength excitation Raman scattering of $Cu_2ZnSn(S_xSe_{1-x})_4$ $(0\leq x\leq 1)$ polycrystalline thin films: vibrational properties of sulfoselenide solid solutions, *Appl. Phys. Lett.*, 2014, **105**, 3, DOI: 10.1063/1.4891333.

22 H. M. Rietveld, A profile refinement method for nuclear and magnetic structures, *J. Appl. Crystallogr.*, 1969, **2**, 65–71, DOI: 10.1107/S0021889869006558.

23 J. Rodriguez-Carvajal and T. Roisnel, https://www.ill.eu/sites/fullprof/.

24 L. Vegard, Gitterschwankungen bei Mischkristallbildung durch Fällung von Lösungen, *Z. Phys.*, 1927, **43**(5), 299–308, DOI: 10.1007/BF01397444.

25 S. Schorr, X-Ray and Neutron Diffraction on Materials for Thin-Film Solar Cells, in *Advanced Characterization Techniques for Thin Film Solar Cells*, ed. D. Abou-Ras, T. Kirchartz and U. Rau, Wiley-VCH Verlag GmbH & Co., 2011, p. 347.

26 J. Tauc, R. Grigorovici and A. Vancu, Optical properties and electronic structure of amorphous germanium, *Phys. Status Solidi*, 1966, **15**, 627–637, DOI: 10.1002/pssb.19660150224.

27 S. P. Bremner, C. Yi, I. Almansouri, A. Ho-Baillie and M. A. Green, Optimum band gap combinations to make best use of new photovoltaic materials, *Sol. Energy*, 2016, **135**, 750–757, DOI: 10.1016/j.solener.2016.06.042.